Materials Advances

ROYAL SOCIETY OF CHEMISTRY

PAPER

View Article Online
View Journal | View Issue

Cite this: *Mater. Adv.*, 2026, 7, 3781

Smartphone-assisted urinary methylmalonic acid sensing using an imidazole-based probe *via* the analyte-triggered aggregation mechanism

Bharat Kaushik, Ajeet Singh, Annu Agarwal, Nancy Punia and Inamur Rahaman Laskar *

Methylmalonic acid (**MMA**) is a key biomarker for vitamin B_{12} deficiency, and its sensing *via* a turn-on-based fluorescence mechanism is less explored. The maximum efficiency reported corresponds to only a few-fold increase in the emission. Similarly, the mechanism by which the emission turns on remains unaccounted for. Here, we report an imidazole-based non-fluorescent probe, **M1**, which turns on blue fluorescence upon the addition of **MMA** due to the 'analyte-triggered aggregation' (ATA) mechanism. An aggregation of probe molecules is triggered by **MMA**, which is mediated by hydrogen bonding and electrostatic interactions between the probe molecules. The probe-analyte interactions and aggregation formation were corroborated by ^{1}H NMR, FTIR, DLS, FESEM, zeta potential measurements, and density functional theory (DFT). The analyte triggered a fluorescence enhancement of the probe of 73-fold (the best reported yet), with an observed detection limit of 5.78 μM. **M1** demonstrated excellent selectivity toward **MMA** over biological interfering elements commonly found in human urine. The scope of **M1** in practical applications was validated by detecting **MMA** in real urine samples, achieving recovery rates of 95–108%. This work presents a detailed sensing mechanism with a cost-effective, non-invasive, and field-deployable strategy (smartphone) for monitoring vitamin B_{12} deficiency *via* **MMA** detection.

Received 18th December 2025,
Accepted 1st March 2026

DOI: 10.1039/d5ma01483b

rsc.li/materials-advances

Introduction

Biomarker detection is crucial for human health, facilitating early disease diagnosis, monitoring, and treatment. Non-invasive methods are increasingly favored over invasive ones for their safety, patient comfort, and accessibility.[1] Although invasive techniques offer in-depth diagnostic information, they are associated with high cost, procedural risk, and discomfort.[2] Non-invasive approaches mitigate these drawbacks, particularly for vulnerable groups like children, the elderly, and patients with comorbidities, while providing affordability and ease of use for widespread healthcare screening.[3]

Methylmalonic acid (**MMA**) is naturally produced in limited quantities in the human body. Elevated **MMA** levels in body fluids, such as serum and urine, are indicative of cobalamin (vitamin B_{12}) deficiency.[4] Vitamin B_{12} serves as a cofactor for methylmalonyl-CoA mutase, which catalyzes the conversion of L-methylmalonyl-CoA to succinyl-CoA in the mitochondrial Krebs cycle. A deficiency in cobalamin disrupts this process, causing the accumulation of methylmalonyl-CoA, which is subsequently converted to **MMA** and excreted in body fluids.[5] Chronic vitamin B_{12} deficiency can lead to irreversible neurological disorders, adverse pregnancy outcomes, and pernicious anaemia.[6] Therefore, early detection of methylmalonic acidemia and aciduria is essential for timely intervention. Studies have shown that healthy individuals have **MMA** concentrations ranging from 73 to 270 nM in serum and 3 to 11 μM in urine.[7]

Conventional methods for **MMA** detection encompass gas chromatography mass spectrometry (GC-MS),[8,9] liquid chromatography mass spectrometry (LC-MS),[10,11] high-performance liquid chromatography (HPLC)[12] and electrochemical techniques.[13,14] Yet, these approaches suffer from drawbacks such as expensive instrumentation, lengthy procedures, and the need for skilled operators. Consequently, there is a pressing demand for rapid, affordable, and real-time alternatives. Fluorescence detection techniques address these needs exceptionally well, delivering high selectivity, sensitivity, and on-the-spot monitoring, making them ideal for biomedical and clinical applications.

Recently, some studies have explored the fluorescence-based detection of **MMA**. For instance, Miyaji *et al.* developed an anthracene-based fluorescent colourimetric sensor that exhibited a green emission turn-on response to **MMA** in urine, although selectivity against other urine components was not

Department of Chemistry, Birla Institute of Technology and Science, Pilani Campus, Vidya Vihar, Pilani, Rajasthan, 333031, India.
E-mail: ir_laskar@pilani.bits-pilani.ac.in

demonstrated.[15] Eu(III)-[16] and Zn(II)[7]-based metal–organic frameworks (MOFs) have also been employed for **MMA** detection using a turn-off fluorescence mechanism. A Cd(II)-based coordination polymer with an amino ligand showed limited fluorescence enhancement and a red shift (~10 nm) in response to **MMA**.[17] Despite these advances, selective turn-on fluorescence sensing of **MMA** remains largely underexplored (Table 3). Additionally, in previous reports, the reason behind the turn-on fluorescence emission has not been thoroughly explained.

Inspired by prior reports[15,17] highlighting the role of hydrogen bonding between a sensing probe and **MMA**, we designed and synthesised an organic probe, **M1**, containing an imidazole ring. The **M1** probe molecule is capable of hydrogen bonding and electrostatic interactions with **MMA**, resulting in **MMA**-triggered aggregation. In this report, we explain the detailed mechanism of turn-on fluorescence *via* the 'Analyte-Triggered Aggregation' (ATA) mechanism[18–20] using different spectroscopic techniques and computational studies. We have also given a thorough explanation for aggregate formation and the most plausible cause of the turn-on emission. **M1** is a synthetically simple, efficient, and selective platform for the on-site, smartphone-based turn-on fluorescence detection method for **MMA** in human urine.

Experimental section

Synthesis and characterization

Synthesis of M1. The synthesis of **M1** was performed in two steps (Scheme 1). In the first step, ortho formylation of 4-hydroxybenzophenone occurs *via* the Duff reaction on both sides, resulting in 5-benzoyl-2-hydroxyisophthalaldehyde (BHP).[21] In the second step, formylated benzophenone, benzil, and ammonium acetate were refluxed overnight in acetic acid, which yields pale green heterocyclic imidazole **M1** (yield 87%).[22] Colourless crystals of **M1** suitable for X-ray diffraction were grown *via* slow evaporation of a hexane-layered dichloromethane (DCM) solution (Fig. S7 SI).

M1 : ^{1}H NMR (400 MHz, Methanol-d_4) δ 8.59 (s, 2H), 7.88–7.85 (m, 2H), 7.71 (s, 4H), 7.67–7.61 (m, 1H), 7.58–7.52 (m, 10H), 7.40–7.30 (m, 8H). ^{13}C NMR (101 MHz, Chloroform-*d*) δ 194.87, 158.38, 144.16, 138.02, 133.01, 132.90, 132.60, 130.16, 129.24, 129.12, 129.04, 128.56.128.35, 128.08, 116.19. HRMS calculated for [**M1** + H]: *m/z* 634.2484 found: [**M1** + H]: *m/z* 634.2492 (Fig. S5 SI).

Results and discussion

Photophysical property studies

UV-Vis spectroscopy was performed in methanol, and the results are presented in Fig. 1a. The spectra reveal two distinct bands: a lower-energy band peaking at around 310 nm (4.00 eV) with a shoulder at 375 nm and another high-energy band centred at around 214 nm (5.79 eV). To investigate the excited-state properties, time-dependent DFT (TD-DFT) calculations were performed. Electronic transitions with notable oscillator strengths (f) were identified (Table 1). The first transition was found at 3.92 eV, but with a vanishingly small oscillator strength ($f = 10^{-4}$), while the second transition was located at 4.07 eV (f = 0.6192), which is in good agreement with the experimental results (4.00 eV). The NTOs for the second transition are shown in Fig. 1d, including the associated CT percentage. The analysis revealed that the transition is primarily composed of local excitations on both imidazole rings and the phenyl ring of benzophenone, as shown in Fig. 1d. We have also observed an $n \rightarrow \pi^*$ charge transfer from the hydroxyl and carbonyl groups to the benzophenone's phenyl ring (see 87.08% charge transfer transition in Fig. 1d). A minor contribution from the diphenyl group to the hole orbital is also observed.

The emission of the probe was extremely weak. The photoluminescence (PL) measurements were performed in methanol using 310 nm (4.00 eV) excitation. The PL experiment revealed two emission bands: a weak high-energy band near 390 nm and a prominent, broad, structureless band centred around

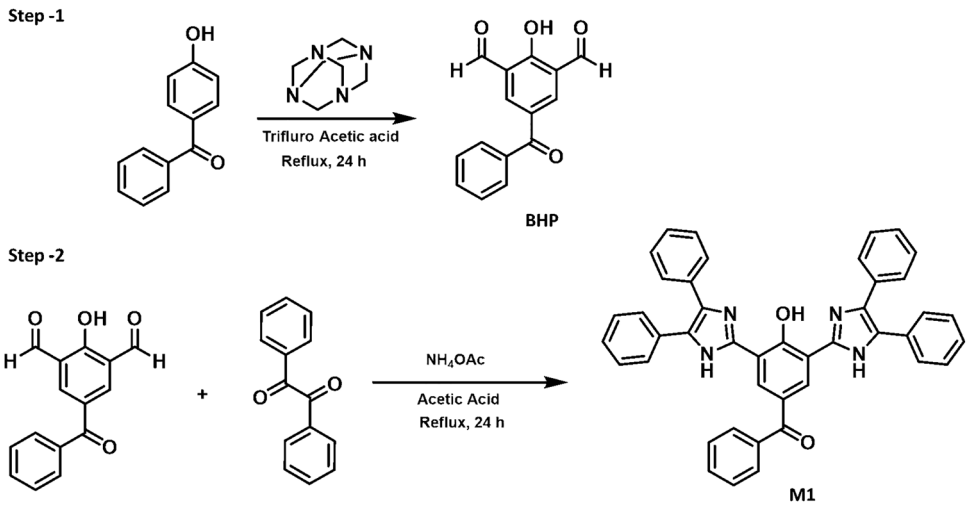

Scheme 1 Synthetic routes and molecular structures of **M1** [(3,5-bis(4,5-diphenyl-1*H*-imidazol-2-yl)-4-hydroxyphenyl) (phenyl)methanone].

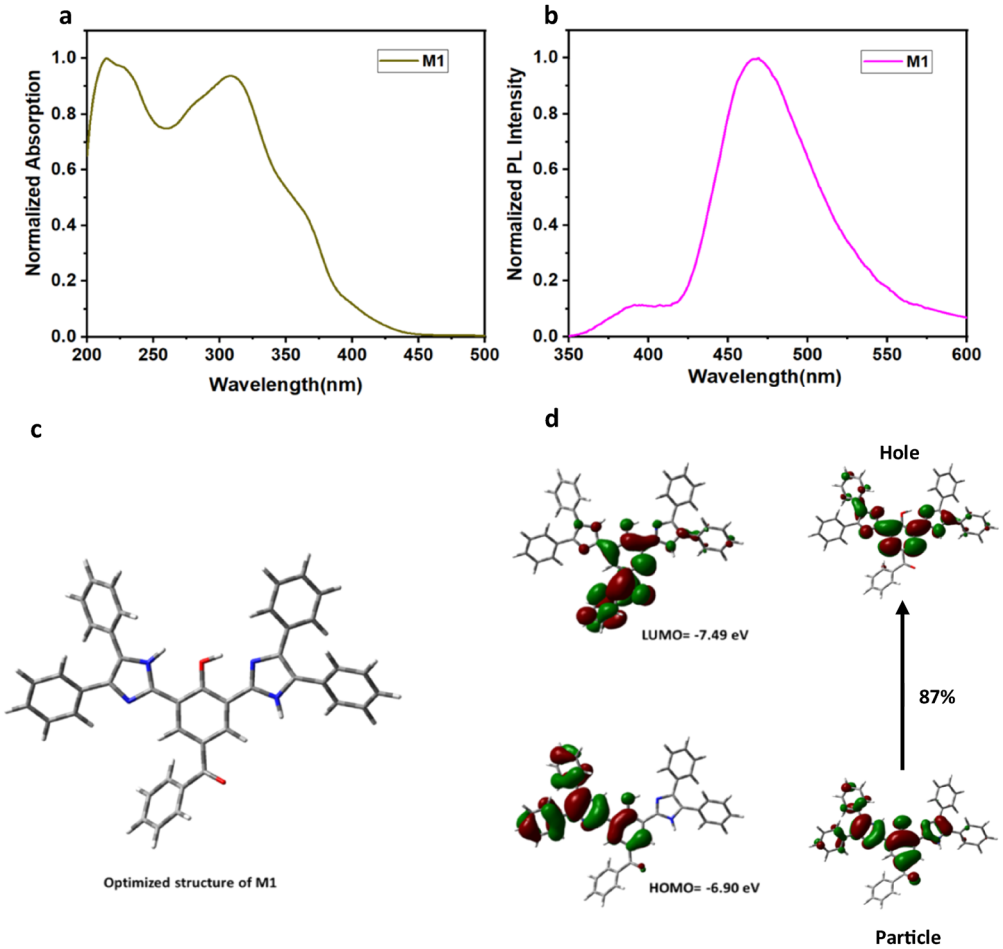

Fig. 1 (a) Absorption and (b) emission (λ_{ex} = 310 nm) spectra of compound **M1** in methanol solvent (10^{-4} M); (c) optimised structure of **M1** using ωb97xd/6-31g(d,p) (functional/basis set); (d) (left) HOMO–LUMO and (right) second transition NTOs of **M1** (here, the particle represents the electron density from which the transition occurs, while the hole represents the region from where the electron density decreases during the transition).

Table 1 Excited state as calculated by TDDFT. The energy and oscillator strength are also provided. The first five transitions are considered for M1 and **M1–MMA–M1**

Transition	Energy (eV)	Oscillator strength (f)
M1		
S_1	3.92	0.0001
S_2	4.07	0.6192
S_3	4.32	0.1713
S_4	4.48	0.4440
S_5	4.59	0.3729
M1–MMA–M1		
S_1	3.88	0.0345
S_2	3.92	0.0813
S_3	4.01	0.1608
S_4	4.07	0.1101
S_5	4.20	0.0682

465 nm (Fig. 1b). The featureless nature of the latter band suggests a CT transition.[23] To validate this, a solvatochromism study was performed, which showed a red shift in emission with increasing solvent polarity, albeit a modest one (Fig. S9, SI). This is consistent with CT behaviour.

MMA sensing

Methylmalonic acid (**MMA**) detection was carried out using both colorimetric and fluorescence methods, employing compound **M1**. A 10^{-4} M methanol solution of **M1** was prepared (lower concentration of **M1** (10^{-5} M) not giving a turn-on response to **MMA** (Fig. S18, SI)), to which 0 to 30 μM aqueous **MMA** was added (30 μL each time), and the mixture was thoroughly mixed. Upon mixing, the solution changed from colourless to pale yellow in daylight and from weak emission to bright blue under a UV lamp (365 nm). This demonstrated a clear turn-on response of **MMA** to our probe, and we proceeded to investigate the sensing mechanism.

The UV-Vis analysis of **MMA** dissolved in the probe was performed in methanol (10^{-4} M). The spectrum showed the emergence of a new band at 415 nm (Fig. 2a) with an isosbestic point at 380 nm, indicating a ground-state interaction between **M1** and **MMA**. The 214 nm and 310 nm absorption bands decreased, while the 415 nm band increased. Such a ratio-metric plot response is very important for real-life sample detection, as it reduces background interference.[24] A change in absorption at 415 nm with increasing concentrations of aqueous **MMA** was also plotted.

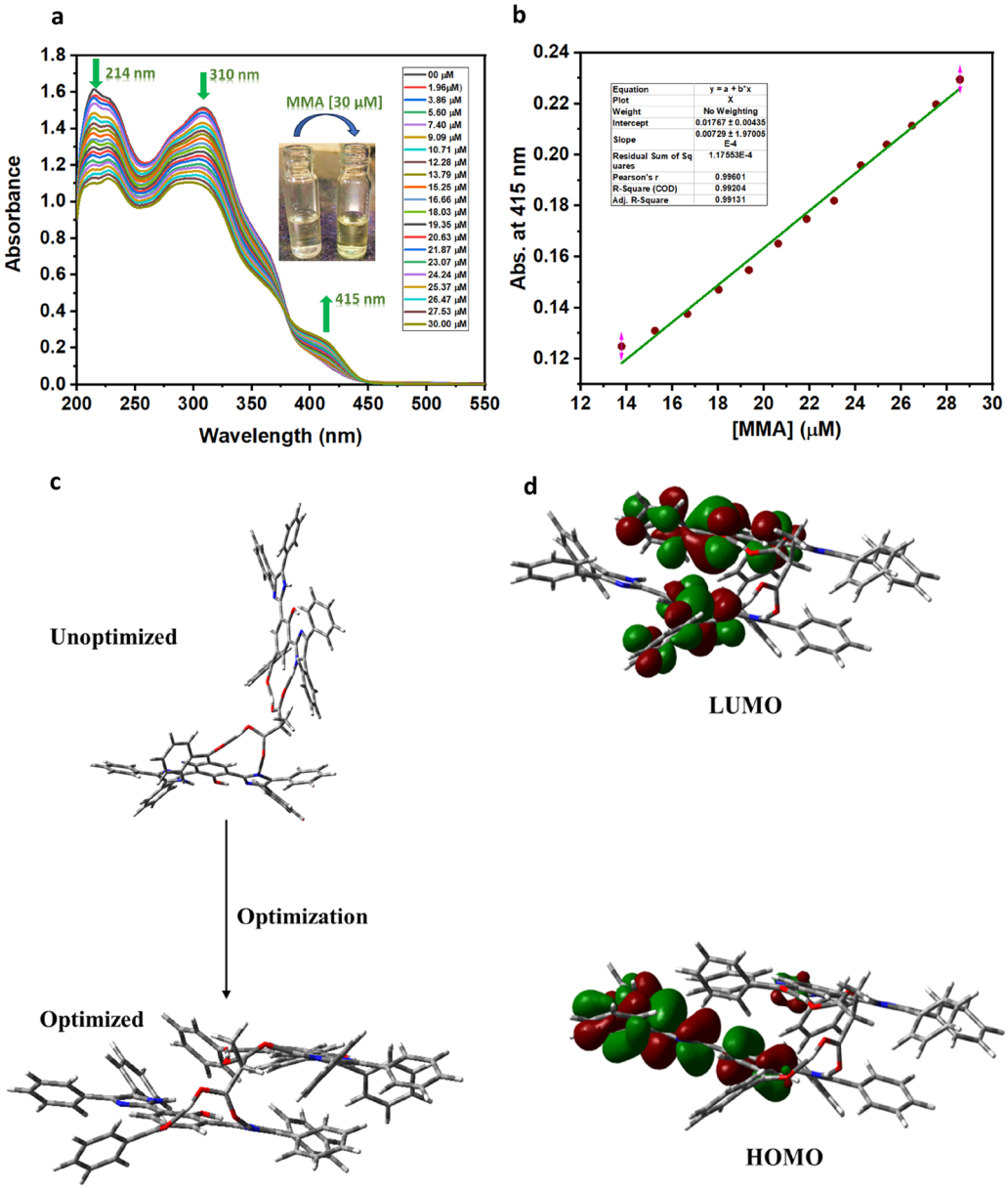

Fig. 2 (a) UV-visible titration of **M1** (10^{-4} M) with aqueous **MMA** concentrations (0 to 30 μM each time 30 μL added) in MeOH medium, an insight image of the same in daylight; (b) linear change in the absorption of **M1** at 415 nm with the amount of aqueous **MMA**; (c) optimized and unoptimized structures of **M1–MMA–M1** by pre-adding the H-bonding interactions; (d) the HOMO and LUMO of optimized **M1–MMA–M1**.

An absorption increment was observed with a nearly 0.99 regression coefficient. The DFT calculations were performed with the probe and the analyte (**MMA**), at the same level of theory as above. NMR corroborated the presence of hydrogen bonding between **M1** and **MMA** (*vide infra* Fig. 6). Based on that, we optimized the **M1–MMA–M1** structure by pre-adding the H-bonding interactions between them (Fig. 2c). Surprisingly, after optimization, **MMA** brought the two **M1** molecules face-to-face (Fig. 2c). This suggested that **MMA** might be inducing aggregation of the molecules. Notably, this significantly impacted the HOMO and LUMO of the molecule, as illustrated in Fig. 2d.

Furthermore, TDDFT calculations revealed that the two low-energy transitions were observed at 3.88 eV and 3.92 eV with oscillator strengths of 0.0345 and 0.0813, respectively (Table 1). Both these transitions are 3 orders of magnitude higher than the probe-only transition at 3.92 eV. Furthermore, the other transitions (S_3 = 4.01, f = 0.1608, and S_4 = 4.07, f = 0.1101) showed a lower oscillator strength as compared to the probe-only transition at 4.07, which had f = 0.6192 (Table 1). This corroborates the above ratio-metric observation from the UV-Vis results.

In the study of fluorescence spectra, initially, a weakly emissive blue-green solution exhibited bright blue fluorescence after the addition of aqueous **MMA** under UV light (365 nm) (Fig. 3a). The PL spectra showed a substantial increase in the emission intensity, approximately 73-fold (in comparison to the

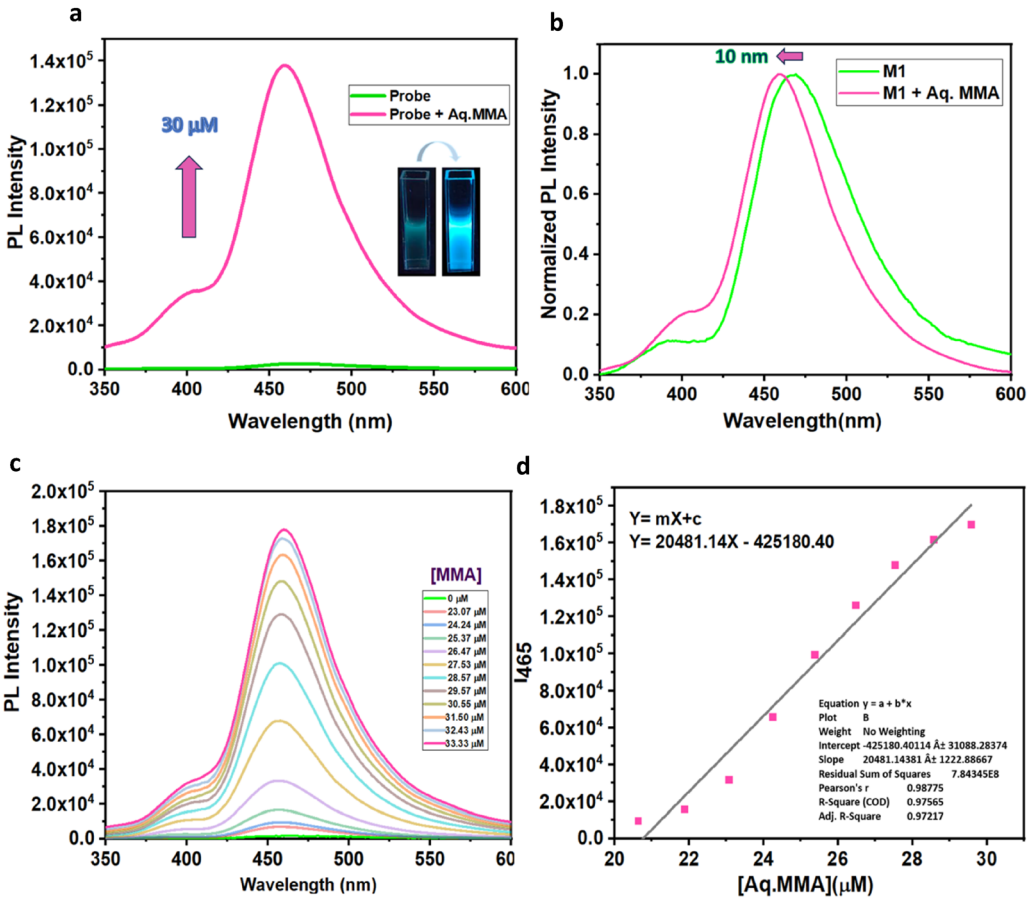

Fig. 3 (a) PL spectrum (λ_{ex} = 310 nm) of **M1** in methanol solvent (10^{-4} M) before and after treatment with aqueous **MMA** (30 μM), at room temperature (25 °C); inset: image of the same under UV light (365 nm); (b) normalized PL spectrum of **M1** before and after treatment with aqueous **MMA**; (c) PL spectra of the **M1** probe solution after titration with different concentrations of aqueous **MMA**; (d) regression plot of the same.

pristine), as calculated by the integrated area under the emission curve. The normalized spectra further confirmed a 10 nm blue shift in emission (Fig. 3b), and no new peak was observed, indicating that the interaction does not induce a new emissive state. Since **M1** is insoluble in pure water, we made two solutions: one, a (9 : 1) water–methanol solution, and the other, a methanol-only solution, to examine the effect of water on **M1**. The PL spectra were then recorded (Fig. S11, SI). The decrease in emission intensity of the water–methanol solution demonstrated that water has no role in intensity enhancement.[25] Also, the (9 : 1) water–methanol solution does not show intensity enhancement upon the addition of **MMA**, as confirmed by emission intensity measurements (Fig. S17, SI). The probable reason is **MMA**'s high-water solubility. A high fraction of water makes **MMA** completely soluble and opposes the formation of the **M1–MMA** complexation. The comparison of reported probes for **MMA** sensing is displayed in Table 3. Thus, **M1** showed a fast response time of 20 seconds and gives a turn-on emission (Table 3 and Fig. S16, SI).

To evaluate the detection sensitivity, a titration experiment was conducted by adding increasing concentrations of aqueous **MMA** to a 10^{-4} M methanol solution of **M1**. As shown in Fig. 3c, the emission intensity increased proportionally with the concentration of **MMA**. Using the standard method based on a signal-to-noise ratio ($3\sigma/S$), the LOD for **MMA** was calculated to be 5.78 × 10^{-6} M. The absolute quantum yield of **M1** was enhanced from 0.07 to 0.51 after the interaction with **MMA**.

Table 2 Detection of **MMA** in real urine samples $\left(\%\,\text{Recovery} = \frac{\text{MMA found}(\mu\text{M})}{\text{MMA added}(\mu\text{M})} \times 100\right)$

Urine samples	**MMA** added (μM)	**MMA** found (μM) ± SD	% Recovery
Sample 1	6.00	6.49 ± 0.18	108.16
Sample 2	10.00	9.86 ± 0.38	98.60
Sample 3	17.80	17.08 ± 0.44	95.95
Sample 4	26.50	25.40 ± 0.14	95.84
Sample 5	35.30	33.83 ± 0.67	95.83
Sample 6	40.10	38.25 ± 0.53	95.38

Selectivity study

Selectivity is a critical factor for the practical application of any sensing system. To assess the selectivity of probe **M1** toward **MMA** in the presence of biologically relevant interfering elements, various analytes commonly found in human urine were tested under identical conditions. The selectivity of the **M1** probe was tested in the presence (Fig. S12 SI) and absence of

Table 3 The comparison between different luminescence sensors of **MMA**. Probe **M1** is synthetically simple, efficient, selective, and highly sensitive turn-on emissive in the presence of **MMA**

S. no.	Probe molecules [coordination polymer (cp)/MOF/organic molecules]	Sensing behaviour	Limit of detection (LOD)	Medium/ solvent	Excitation/ emission wavelength (nm)	Quantum yield (%)	Stokes shift (nm)	Response time (seconds)	Application	Ref.
1.	[Cd(bbip)(NH_2-BDC)(H_2O)]	Red shift with turn-on fluorescence	0.72 μM	EtOH	370/422	—	52	300	Urine	17
2.	Ru/Tb-MOF	Ratiometric fluorescence	3.8 μg mL^{-1}	—	366/545 and 585	—	79 and 19	60	Urine	37
3.	Zn-MOF	Turn-off fluorescence	1.7 nM	H_2O	290/350	—	60	30	Urine	7
4.	Eu-MOF	Turn-off fluorescence	0.107 μM	—	468/525	1.53	57	120	Urine	16
5.	$^{35}_{n}$ {[Co(L)(bimb)]}$_n$	Turn-off fluorescence	1.76 μM	H_2O	275/400	—	125	—	Urine	35
	{[Co(L)$(bimb)_{1/2}$]}$_n$		1.03 μM		270/375	—	105	—	Urine	
			0.18 μM		270/380	—	110	—	Urine	
6.	{[Co(L)(bibp)]bibp·$2H_2O$}$_n$	Turn-on fluorescence	9.86 μM	—	275/385	—	110	—	Urine	38
7.	Molecular sensor 2	Turn-on fluorescence	1 μM	1% DMSO in ACN	340/512	—	172	—	Urine	15
8.	**M1**	Turn-on fluorescence	5.78 μM	MeOH	310/465	7	155	20	Urine	This work

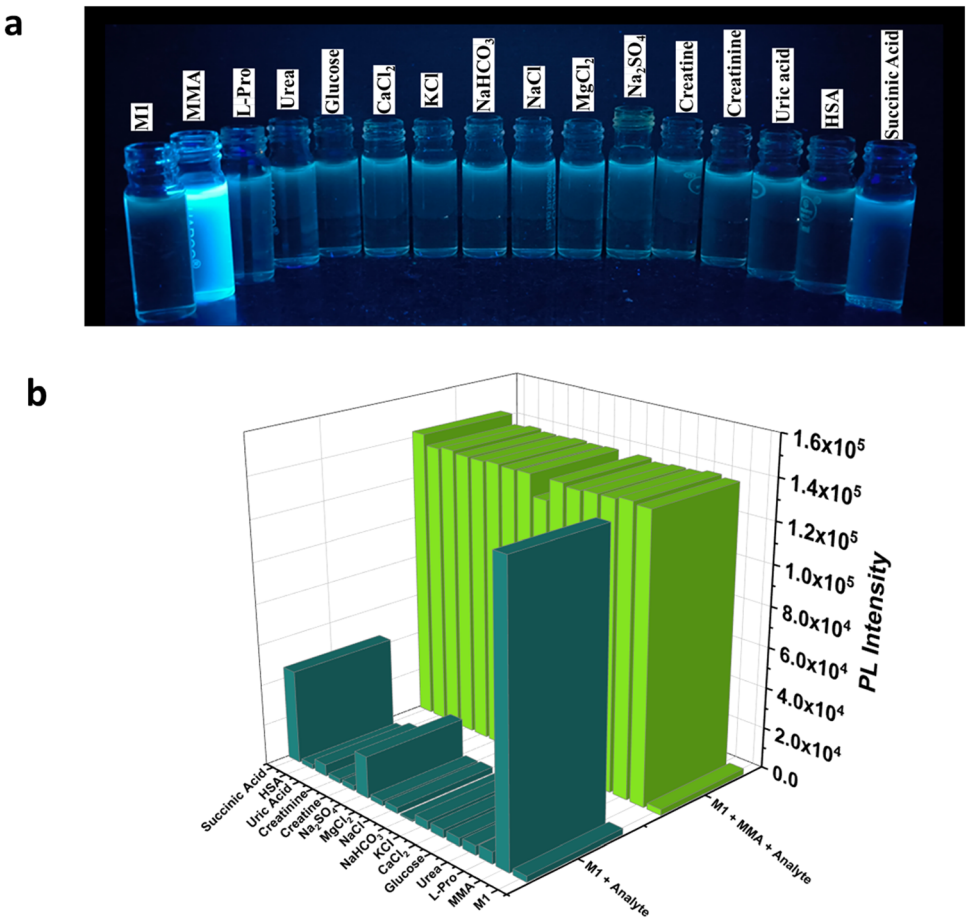

Fig. 4 (a) Photograph of the methanol solution of the **M1** probe under a UV lamp (365 nm) after the addition of an aqueous solution of different urine constituents like **MMA**, L-proline, urea, glucose, $CaCl_2$, KCl, $NaHCO_3$, NaCl, $MgCl_2$, Na_2SO_4, creatine, creatinine, uric acid, human serum albumin (HSA), and succinic acid; (b) Bar graph showing the PL Intensity of **M1** with different analytes (λ_{ex} = 310 nm) with (green colour), and without **MMA** (purple colour).

MMA (Fig. 4a). A 10^{-4} M methanol solution of **M1** (2 mL) was treated with 100 μM of each analyte, including **MMA** (30 μM) and other species (present in urine) like L-proline, urea, glucose, $CaCl_2$, KCl, $NaHCO_3$, NaCl, $MgCl_2$, Na_2SO_4, creatine, creatinine,

uric acid, human serum albumin (HSA), and succinic acid. The PL intensity at 465 nm was used as the response metric using a 310 nm excitation (Fig. 4). The results demonstrated that none of the other analytes caused significant fluorescence enhancement apart from **MMA**, highlighting the high selectivity and robustness of **M1** for **MMA** detection, even in complex biological matrices such as urine.

FTIR and NMR: hydrogen bonding between M1 and MMA

To investigate the interaction between probe **M1** and **MMA**, FT-IR analysis was conducted on **M1** and **MMA** (Fig. 5). The **M1** spectrum showed peaks at 1650 and 1603 cm^{-1}, along with a high-energy broad peak at 3200–3500 cm^{-1} (O–H and N–H). The 1650 cm^{-1} and 1603 cm^{-1} peaks were assigned to C═O and C═N stretches, respectively.[26] For **MMA**, a low-energy vibration at 1720 cm^{-1} (C═O) was observed, along with a high-energy broad signal of OH stretching in the 3300–3400 cm^{-1} region. FTIR was also performed for the combined probe analyte complex (**M1–MMA**) (Fig. 5). C═O stretches showed a redshift from 1650 to 1639 (**M1**) and from 1720 to 1702 cm^{-1} (**MMA**). This clearly indicates a weakening of the C═O bond,[27] likely due to hydrogen bonding. Furthermore, the N–H and O–H stretches of **M1** and **MMA** disappeared, indicating the involvement of N–H (**M1**) and O–H (**MMA**).[28] This proves the existence of H-bonding between **M1** and **MMA**.

Next, to investigate the exact interaction between hydrogen and oxygen, a ^{1}H NMR titration was performed in the CH_3OD solvent. First, a ^{1}H NMR spectrum of the probe (**M1**) was recorded in the presence of 2 equivalents of **M1** to establish the baseline chemical shift under reference conditions. Subsequently, 1 equivalent of **MMA** was added to the same NMR tube while maintaining a constant volume, mixed thoroughly, and a second ^{1}H NMR spectrum was acquired to observe the analyte-induced chemical shift. The ^{1}H NMR spectra (Fig. 6b) showed both shielding and deshielding effects upon the addition of **MMA**. Notably, the H_d protons (–NH, see Fig. 6a) of **M1** were deshielded after the addition of 1 equivalent of **MMA**, suggesting their direct involvement in binding with the analyte. Furthermore, the aromatic protons of **M1** also shifted: H_b and H_c protons were deshielded, while the H_a proton was shielded. These changes are attributed to the altered electronic environment and the distinct ring currents due to the non-coplanar orientation of the phenyl rings.[29] The H_{OH} proton signal was not observed, likely due to the exchange with the trace amounts of moisture present in CD_3OD, which was further confirmed by recording the ^{1}H NMR spectra in the DMSO-d_6 solvent (Fig. S6 SI).[30]

Upon addition of aqueous **MMA**, the analyte appears to participate in intermolecular hydrogen bonding with a nitrogen atom in **M1**. The stoichiometry of the **M1–MMA** interaction was further examined using Job's plot (Fig. S14 SI). For this, 10^{-4} M methanolic solutions of **M1** and **MMA** were mixed in varying mole fractions while maintaining a constant total volume of 2 mL. The absorption spectra were recorded for each mixture (Fig. S14a SI), and a plot of absorbance *versus* the molar fraction of **M1** showed a maximum at a 0.7 molar fraction (at 415 nm). This indicates a ~2 : 1 stoichiometric ratio of **M1** to **MMA**, confirming the formation of an **M1–MMA** complex. Time-resolved fluorescence spectroscopy was also performed for **M1** and the **M1–MMA** mixture. The lifetime of **M1** (0.14 ns) decreases (0.11 ns) after the interaction with **MMA** (Fig. S10, SI).

Thus, corroborating our hypothesis of the presence of H-bonding between **M1** and **MMA**. This was used to carry out **M1–MMA–M1** DFT calculations in the previous section and validates the computational results based on H-bonding. Next, we explore the role of this H-bonding in the formation of aggregates in the **M1–MMA** solution.

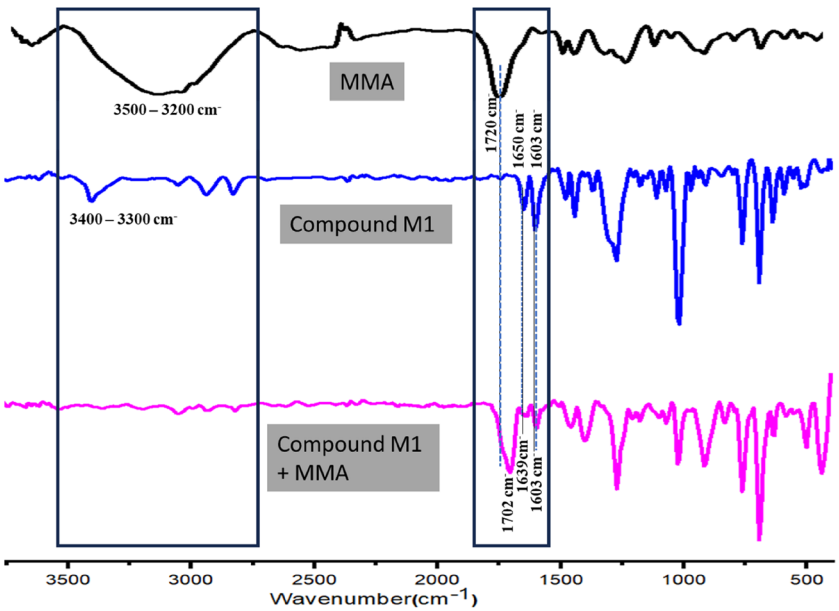

Fig. 5 FT-IR spectra of compound **M1**, **MMA**, and **M1 + MMA**.

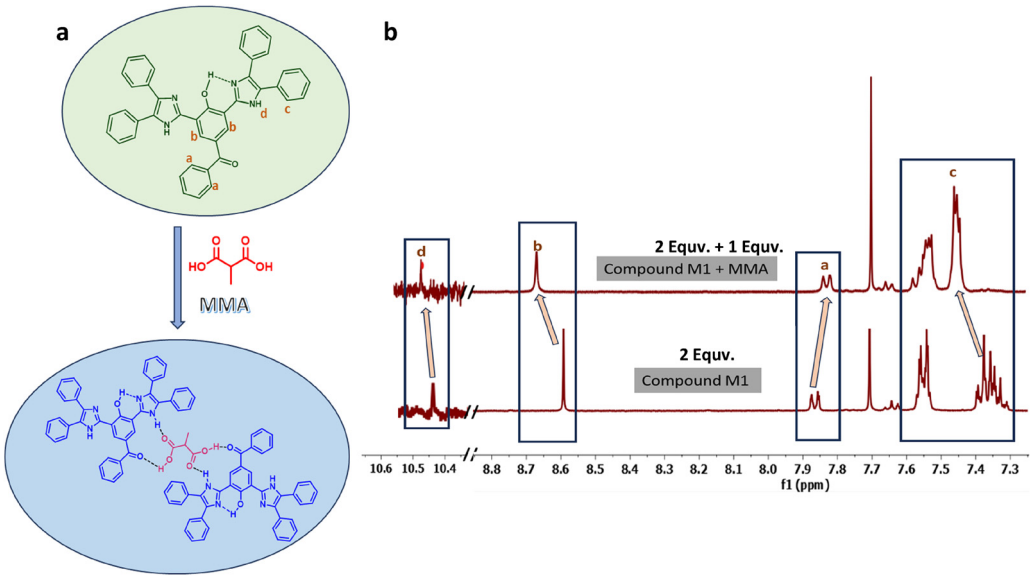

Fig. 6 (a) Schematic representation shows the interactions between the **M1** compound and **MMA**; (b) ^{1}H-NMR spectra of compound **M1** (1 equiv.) and **MMA** (2 equiv.) in the CD_3OD solvent.

Analyte triggered aggregation (ATA): DLS, FESEM and zeta potential study

To investigate the ATA mechanism, we performed dynamic light scattering (DLS), field-emission scanning electron microscopy (FESEM) analysis, and zeta potential measurements of the probe to demonstrate aggregate formation after the addition of the analyte (**MMA**) (Fig. 7). From the DLS data, it is evident that as **MMA** (30 μM) is added to the **M1** probe solution, the average particle size increases from 667.14 nm to 1534.33 nm. Additionally, DLS measurements exhibit a uniform PDI (<0.4) with a narrow distribution of particles (Fig. 7). FESEM images of **M1** and **M1–MMA** also confirm the aggregate formation in the solid state in the presence of **MMA**. In the FESEM of **M1** (Fig. 7a), the particles are round in shape with an average particle size of 438.8 nm. After the addition of **MMA**, the particles of **M1** aggregated with an average particle size of 2.94 μm (Fig. 7b).

Both DLS and FESEM confirmed the formation of analyte-triggered aggregates. One additional experiment was also performed to support the **MMA**-triggered aggregation formation by diluting the **M1–MMA** solution from 10^{-4} M to 10^{-7} M with methanol (Fig. S15, SI). The emission intensity of the solution decreases with dilution, suggesting a decrease in the aggregation.

The zeta potential of **M1** before and after the addition of **MMA** was measured with a narrow zeta potential distribution (Fig. S13 SI). The average zeta potential of **M1** and **M1–MMA** was measured to be +14.4 mV and +6.9 mV, respectively (Fig. 8).

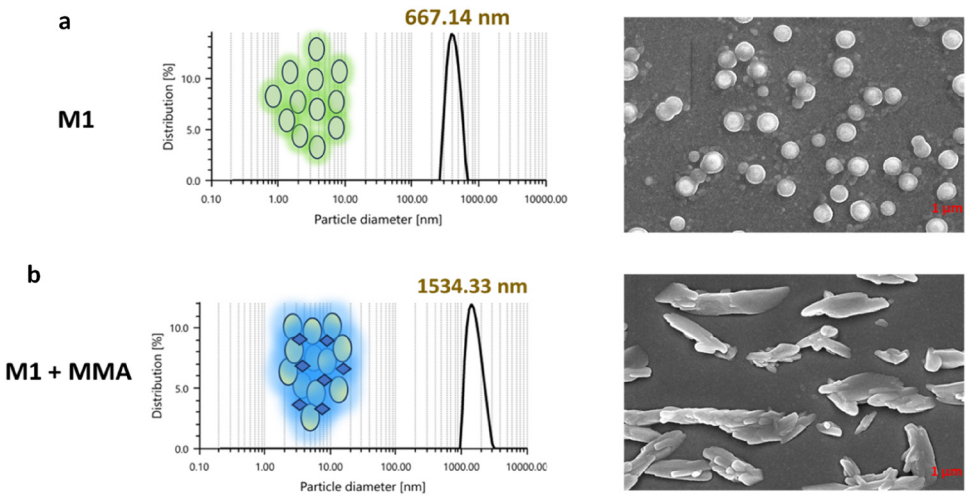

Fig. 7 (a) DLS spectrum (left side) (inset: representation of **M1** molecules without **MMA**) and the FESEM image (right side) of the **M1** probe without **MMA**; (b) DLS spectrum (left side) (inset: representation of **M1** with **MMA**) and the FESEM image (right side) of the **M1** probe in the presence of **MMA**.

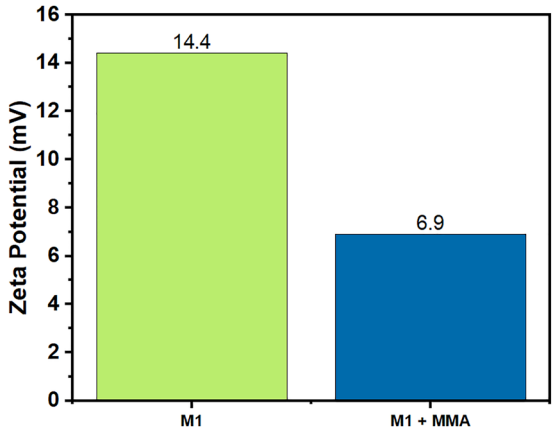

Fig. 8 Zeta potential of **M1** and **M1–MMA** solutions.

Methyl malonic acid contains a –COOH group, which partially has a negative charge. The electrostatic interaction between **M1** and **MMA** decreases the overall positive charge. A change in the positive zeta potential suggests the aggregation of **M1** induced by **MMA**.[31–33] All these experiments demonstrate that **MMA** is responsible for inducing aggregation mediated by hydrogen bonding with the probe **M1**.

MMA sensing in human urine

We have also evaluated the **M1** probe for detecting **MMA** in human urine samples. To quantify unknown **MMA** concentrations, a calibration curve was first established by plotting fluorescence intensity against known **MMA** concentration (Fig. 9b). The spiked recovery method was employed for detection.[34] The changes in the emission intensity were observed under a UV lamp (λ_{ex} = 365 nm) after treating the **M1** solution with **MMA**-spiked urine samples (Fig. 9a).

The six urine samples, collected from the BITS Medical Centre, BITS Pilani, were centrifuged at 3000 rpm for 10 minutes to remove suspended particles. The resulting supernatant was spiked with known **MMA** concentrations. For each measurement, 30 μL of spiked urine was added to 2 mL of a 10^{-4} M **M1** solution in methanol (Fig. 9c), and the fluorescence emission was recorded. **MMA** concentrations were then determined using the calibration curve. The recovery results, shown in Table 2, ranged from 95% to 108%, demonstrating the probe's effectiveness in detecting **MMA** in real urine samples and are comparable to literature reports.[7,35]

Low-cost MMA detection on a TLC strip using a smartphone

Based on earlier discussions, it is necessary to accurately measure **MMA** in urine for monitoring vitamin B_{12} deficiency.

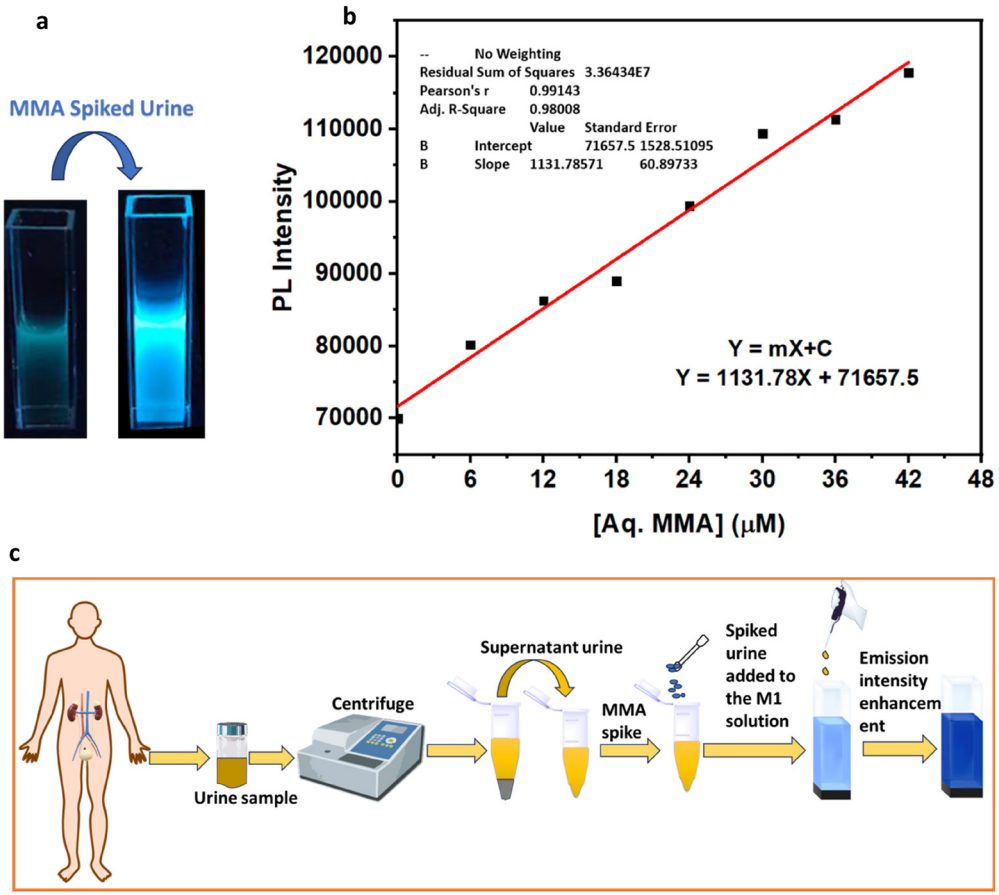

Fig. 9 (a) Image of the **M1** probe solution (10^{-4} M) after being treated with an **MMA** spiked (30 μM) urine sample (under a UV-lamp); (b) calibration curve of the **M1** probe after being treated with different concentrations of aqueous **MMA**; (c) the scheme shows the urine sample and its pre-treatment.

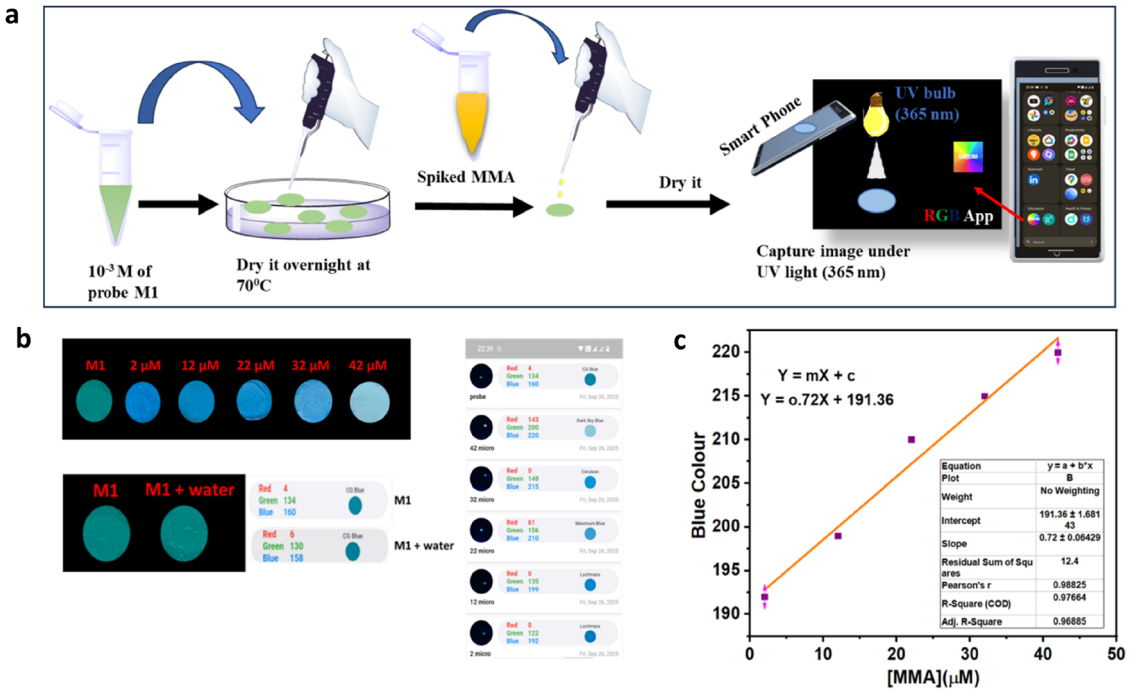

Fig. 10 (a) The scheme shows the preparation of the **M1**-coated TLC strip and captures the image from a smartphone RGB camera under a UV lamp after being treated with different spiked concentrations of **MMA** in urine; (b) TLC strip image (left) along with blue colour intensities (right) captured using a smartphone RGB camera after being treated with different **MMA** concentrations along with the control experiment (only water); (c) blue colour *versus* **MMA** concentration in the range of 2 to 42 μM concentration.

However, advanced path lab facilities are mostly unavailable in remote areas for rapid on-site **MMA** detection. To overcome this, an alternative method using a ''chemically modified TLC strip'' was developed, which abolishes the complex instrumentation requirement, tedious sample preparation, and specialized personnel. The **M1**-coated TLC strip showed no colour in daylight but a light green colour under hand-held UV light (365 nm) (Fig. 10b). The colour changes from green to blue on the addition of spiked **MMA** urine under a UV lamp. The intensity of blue fluorescence increases with **MMA** concentration. The control experiment was also performed in the presence of water only, and it was found that there was no significant change in blue colour intensity (Fig. 10b). When the strips were treated with 20 μL of different **MMA** concentrations, a dependent intensity of blue-coloured fluorescence was observed. The blue colour intensity was captured using a smartphone RGB camera in a black box (Fig. 10a). The colours (red, green, and blue) on the standard RGB scale are represented by whole numbers ranging from 0 to 255. The number [255,255,255] on the scale denotes true white, while [0,0,0] denotes absolute black.[36] The result shows that the blue colour intensity increases gradually with increasing **MMA** concentration. By considering the blue colour intensity as a signal, a linear trend was observed between **MMA** concentration and blue colour. The blue colour intensity is linear (R^2 = 0.9766) in the concentration range of 2 to 42 μM (Fig. 10c). These results suggest that the detection of **MMA** in an ''on-site'' way is possible using a smartphone.

Conclusions

In summary, we have synthesized a new imidazole-functionalized organic fluorescent probe, **M1**, in a convenient route capable of selectively detecting **MMA** through a turn-on mechanism. The emission intensity increased by about 73-fold, which is the best reported to date. The sensor operates *via* ATA formation, supported by hydrogen bonding interactions and electrostatic interactions between the **M1** and **MMA**, as confirmed by FTIR, ^{1}H NMR spectroscopy, DLS, FESEM, and zeta potential measurements. This ATA (analyte-triggered aggregation) led to the formation of a new lowest excited state, as confirmed by the formation of a new band in the UV-Vis spectrum and TDDFT results. This new state leads to turn-on emission, confirming the ATA-mediated emission. The complex formation displayed ~2 : 1 (**M1**: **MMA**) stoichiometry, as confirmed by Job's plot analysis. **M1** exhibited pronounced fluorescence enhancement with a low detection limit of 5.78 μM, enabling trace-level **MMA** sensing. It also supports low-cost, on-site detection *via* TLC plate-based imaging on a smartphone. Notably, **M1** showed excellent selectivity over common urinary analytes and accurately quantified **MMA** in spiked human urine (95–108%). This non-invasive, user-friendly method holds strong promise for rapid point-of-care screening for vitamin B_{12} deficiency-related metabolic disorders.

Conflicts of interest

There are no conflicts to declare.

Data availability

The data supporting this article have been included as part of the supplementary information (SI). The supplementary information contains instrumentation, methodology, NMR, HRMS, crystal structure, experimental data, and additional supporting data. See DOI: https://doi.org/10.1039/d5ma01483b.

CCDC 2455842 contains the supplementary crystallographic data for this paper.[39]

Acknowledgements

This work was supported by the Department of Biotechnology (DBT), Govt. of India (project number: BT/PR33133/MED/32/704/2019) for financial assistance, and the UGC sponsored Special Assistance Programme (F.540/14/DRS/2007, SAP-I) and DST-FIST (SR/FST/CSI-270/2015) for the HRMS facility in the Department of Chemistry, BITS Pilani. The authors are grateful to the Medical Centre, BITS Pilani, Pilani Campus, for providing the urine samples.

References

1 S. Zakari, N. K. Niels, G. V. Olagunju, P. C. Nnaji, O. Ogunniyi, M. Tebamifor, E. N. Israel, S. E. Atawodi and O. O. Ogunlana, *Front. Oncol.*, 2024, **14**, 1405267.
2 J. Hernandez Roman and M. S. Siddiqui, *Endocrinol., Diabetes Metab.*, 2020, **3**, e00127.
3 K. Lazaros, S. Adam, M. G. Krokidis, T. Exarchos, P. Vlamos and A. G. Vrahatis, *Sensors*, 2025, **25**, 1396.
4 D. J. Harrington, in *Laboratory Assessment of Vitamin Status*, ed. D. Harrington, Academic Press, 2019, pp. 265–299, DOI: 10.1016/B978-0-12-813050-6.00012-7.
5 W. Zhou, H. Li, C. Wang, X. Wang and M. Gu, *Front. Genet.*, 2019, **9**, 726.
6 M. J. Shipton and J. Thachil, *Clin. Med.*, 2015, **15**, 145–150.
7 X. Zhang, Y. Tian, J. Shi, X. Kang and Z. Liu, *J. Mater. Chem. C*, 2022, **10**, 12821–12828.
8 Ø. Midttun, A. McCann, O. Aarseth, M. Krokeide, G. Kvalheim, K. Meyer and P. M. Ueland, *Anal. Chem.*, 2016, **88**, 10427–10436.
9 M. Aghamohammadi, P. Shahdousti and B. Harooni, *Microchem. J.*, 2016, **124**, 188–194.
10 V. M. Carvalho and F. Kok, *Anal. Biochem.*, 2008, **381**, 67–73.
11 N. Sriboonvorakul, N. Leepipatpiboon, A. M. Dondorp, T. Pouplin, N. J. White, J. Tarning and N. Lindegardh, *J. Chromatogr. B:Anal. Technol. Biomed. Life Sci.*, 2013, **941**, 116–122.
12 T. Bito, Y. Matsunaga, Y. Yabuta, T. Kawano and F. Watanabe, *FEBS Open Bio*, 2013, **3**, 112–117.
13 K. B. Akshaya, V. Anitha, M. Nidhin, Y. N. Sudhakar and G. Louis, *Talanta*, 2020, **217**, 121028.
14 Z. K. Shihabi and M. A. Friedberg, *Electrophoresis*, 1997, **18**, 1724–1732.
15 H. Miyaji, J. Fujimoto, R. Mabuchi, M. Okumura, S. Goto and Y. Honda, *Tetrahedron Lett.*, 2017, **58**, 3623–3627.
16 X. Lu, Y. Tang, G. Yang and Y.-Y. Wang, *J. Mater. Chem. C*, 2023, **11**, 2328–2335.
17 W.-H. Xu, S.-L. Yao, X.-C. Xie, P. Wen, J.-Y. Zhong, J.-Y. Ding, R.-H. Wu, J.-L. Lin, H. Liu and S.-J. Liu, *J. Mol. Struct.*, 2025, **1323**, 140758.
18 Z. Yao, H. Bai, C. Li and G. Shi, *Chem. Commun.*, 2010, **46**, 5094–5096.
19 H. Dong, F. Zou, X. Hu, H. Zhu, K. Koh and H. Chen, *Biosens. Bioelectron.*, 2018, **117**, 605–612.
20 J.-H. Lin and W.-L. Tseng, *Talanta*, 2015, **132**, 44–51.
21 F. Aldabbagh, in *Comprehensive Organic Functional Group Transformations II*, ed. A. R. Katritzky and R. J. K. Taylor, Elsevier, Oxford, 2005, pp. 99–133, DOI: 10.1016/B0-08-044655-8/00048-9.
22 N. Farahani, K. Zhu, N. Noujeim and S. J. Loeb, *Org. Biomol. Chem.*, 2014, **12**, 4824–4827.
23 J. C. G. Bünzli, in *Reference Module in Materials Science and Materials Engineering*, Elsevier, 2016, DOI: 10.1016/B978-0-12-803581-8.01855-5.
24 Z. Wang, L. Zhang, Y. Hao, W. Dong, Y. Liu, S. Song, S. Shuang, C. Dong and X. Gong, *Anal. Chim. Acta*, 2021, **1144**, 1–13.
25 J. Devasia, F. Joy and A. Nizam, *Chem. - Eur. J.*, 2023, **29**, e202203652.
26 L. Ren, J. Wang, X. Meng, C. Liu, Z. Liao and D. Zhang, *Inorg. Chim. Acta*, 2025, **583**, 122705.
27 L. Paoloni, A. Patti and F. Mangano, *J. Mol. Struct.*, 1975, **27**, 123–137.
28 K. N. Blodgett, J. L. Fischer, T. S. Zwier and E. L. Sibert, *Phys. Chem. Chem. Phys.*, 2020, **22**, 14077–14087.
29 J. Mruk, L. Pazderski, J. Ścianowski and A. Wojtczak, *Inorg. Chim. Acta*, 2020, **500**, 119182.
30 F. Bonaldo, F. Mattivi, D. Catorci, P. Arapitsas and G. Guella, *Molecules*, 2021, **26**, 3544.
31 X. Jiang, H. Jin, Y. Sun and R. Gui, *Microchim. Acta*, 2019, **186**, 580.
32 S. Tanvir, S. Pulvin and W. Anderson, *MOJ Toxicol.*, 2015, **1**, 00011.
33 T. Yuan, L. Gao, W. Zhan and D. Dini, *Pharm. Res.*, 2022, **39**, 767–781.
34 D. Thakur, N. P. Dubey and R. Singh, *Crit. Rev. Anal. Chem.*, 2024, **54**, 2053–2071.
35 R. Luo, C.-G. Xu, D.-M. Zhang, L.-L. Wang, R.-X. Wu, G.-B. Chen, P. Lu, Y.-H. Fan and F. Shao, *Talanta*, 2023, **265**, 124803.
36 X. Liu, R. Gao, L. Han, C. Kan and J. Xu, *Talanta*, 2023, **252**, 123849.
37 Y. Zhang, X. Qu and B. Yan, *J. Mater. Chem. C*, 2021, **9**, 3440–3446.
38 R. Luo, C.-G. Xu, H.-J. Yu, R.-X. Wu, P. Lu, Y.-H. Fan and F. Shao, *CrystEngComm*, 2023, **25**, 4120–4125.
39 CCDC 2455842: Experimental Crystal Structure Determination, 2026, DOI: 10.5517/ccdc.csd.cc2nfhqb.